I&EC research
Industrial & Engineering Chemistry Research

pubs.acs.org/IECR

Article

Flow Reconstruction and Prediction Based on Small Particle Image Velocimetry Experimental Datasets with Convolutional Neural Networks

Likun Ma, Sina Kashanj, Shuliang Xu, Jibin Zhou,* David S. Nobes, and Mao Ye*

Cite This: *Ind. Eng. Chem. Res.* 2022, 61, 8504−8519

Read Online

ACCESS | Metrics & More | Article Recommendations

ABSTRACT: Particulate two-phase flows normally manifest high dimensional and complex nonlinear flow phenomena. To capture the intrinsic characteristics of the fluid flows, dimension reduction and feature capturing are of fundamental importance. In this work, we focused on the flow reconstruction and prediction based on dimension reduction and feature capturing with small noised datasets obtained by particle image velocimetry (PIV) experiments by use of a skip-connection convolutional neural network based on autoencoder (*sc*CAE). We evaluated the performances of *sc*CAE in reconstructing and predicting the high dimensional and nonlinear flows around a single particle for moderate Reynolds numbers (*Re*) of 400−1400. It is shown that *sc*CAE with the latent vector size of four can well reconstruct and predict the fluid flow fields around either a sphere or cube based on the small noised PIV datasets with the data size of several hundreds, which suggests the robustness and generality of *sc*CAE in dimension reduction and feature capturing. This may be extended to wider applications in extracting dimension-reduction latent vectors from limited ground truth experimental PIV data and disclosing the inherent physics.

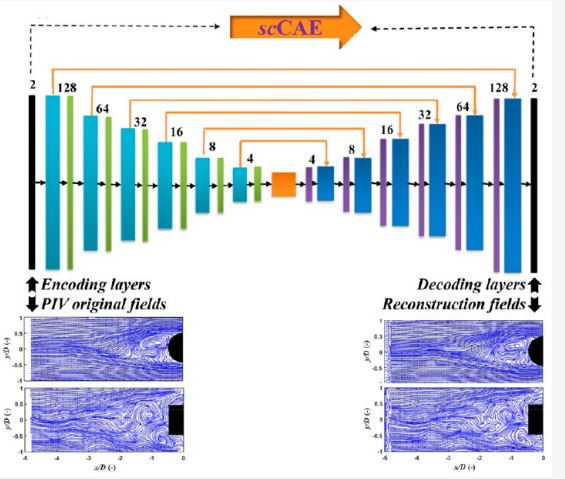

1. INTRODUCTION

Flows around a single particle is of fundamental importance in understanding and controlling the multiphase processes such as catalytic reactors, coal combustors and pneumatic conveying.[1] However, such fluid flows are affected by particle shape, Reynolds number (*Re*) and among many others,[2,3] and manifest quite involved characteristics. For instance, a spherical particle has a smooth and continuous surface and demonstrates flow separation at varying locations dependent upon *Re*, while a cubic particle shows flow separation at fixed points in the leading edges due to the sharp surfaces.[4] Despite the significant impacts on interphase heat and mass transfer, the characteristics of fluid flow around a single particle of different shapes, such as wake structures, are yet to be fully understood.

Particle image velocimetry (PIV)[4−7] is a nonintrusive technique for quantitatively measuring the spatial flow velocity distribution based on the fine tracers well seeding the fluid.[8] PIV has been considered as one of the most effective methods for studying the fluid flow around a single particle.[4,5,9,10] For example, Cate et al. used PIV to measure the flow fields around a single sphere settling under gravity for *Re* ranging from 1.5 to 31.9, in which the maximal frame rate of 250 Hz was achieved to obtain an image of 512 × 512 pixels with a total of 961 vectors per image.[9] Hajimirzaie et al. applied PIV with a frame rate of 7.2 Hz to achieve a spatial resolution of 0.55 mm in their study on the fluid flow around a wall-mounted sphere in a thin laminar boundary layer at *Re* = 17 800.[11] Klotz et al. investigated the flow characteristics behind a single cube with a face normal to the flow for 100 ≤ *Re* ≤ 400 and the PIV measurements with 15 Hz were conducted to obtain snapshots of 1600 × 1200 pixels for each *Re*.[5] Khan et al. studied the fluid flow around a cube placed either normal[4] or at an angle of 45°[10] to the freestream with *Re* of 500−50000, in which the PIV with a frame rate of 1 Hz was used to obtain the images of 1024 × 1392 pixels. As can be found, most of the PIV measurements discussed above were performed at a relatively lower frame rate in order to achieve a higher spatial resolution. In fact, it is a challenge to get fluid flows of both a high spatial resolution and a high frequency in PIV measurements. Obtaining a large high-frequency time series of flow field

Special Issue: Machine Learning and Data Science in Chemical Engineering

Received: November 30, 2021
Revised: February 20, 2022
Accepted: February 23, 2022
Published: March 4, 2022

https://doi.org/10.1021/acs.iecr.1c04704
Ind. Eng. Chem. Res. 2022, 61, 8504−8519

data with a high spatial resolution by PIV measurements, if not impossible, is quite costly, which causes a challenge for obtaining a big dataset.

However, the characteristics for fluid flow around a single particle (for instance, the wake structure evolutions) are transient and high-dimensional, showing the chaotic and complicated nonlinear nature. Therefore, one of the nontrivial tasks is to capture the key structures and features embedded in the time series of flow fields and gain insights into the underlying mechanisms. This is particularly essential for constructing the control equations and generalizing the understanding of fluid dynamics of flows around single particles under different conditions. The dimension reduction methods that can capture the key structures and features of flow fields have been widely used in this connection. Typical examples include the proper orthogonal decomposition (POD)[12] and dynamic mode decomposition (DMD)[13] methods, in which the transient flow fields are decomposed into a series of linear expansions and/or orthogonal bases.[14] However, these traditional linear methods were not suitable for dimension reduction and features capturing of the flow fields around a single particle (especially under high *Re*) due to the highly nonlinear nature of the fluid flows.

With the rapid development of computational science, the machine learning methods have been extensively applied to study complicated high-dimensional and nonlinear fluid flows.[15] On the one hand, the machine learning methods show a robust ability on the end-to-end fluid motion estimation problem by extracting velocity fields from original fluid images, acting as the role of cross-correlation algorithms.[16−19] On the other hand, the machine learning methods also show great potential on feature extractions of spatiotemporal-resolved flow fields based on dimension reduction. In particular, the convolutional neural networks (CNNs) models, which rely essentially on the availability of big data as the input for training and can naturally take into account the spatial structure of fluid flows, have shown huge potential on dimension reduction and features extraction for complicated flow fields.[20] CNNs can eliminate redundant parameters compared to the normal neural networks, because of the inclusion of parameter-sharing with a filtering kernel convolving across the domain to learn the correlation structure in the dataset.[21−23] Since the same parameters are reused (shared) in convolutions across the spatial domain, the number of parameters needed in CNNs can be orders of magnitude fewer than that of the fully connected neural networks. This feature makes CNNs quite attractive in spatially coherent information extraction[24,25] and dimension reduction for complex fluid flows.[14,26,27] A CNNs-based autoencoder (CAE) was thus proposed to reduce the dimensions in a two-dimensional airfoil flow and the latent vector learned by CAE was found capable reflecting the main features of flow fields over time.[27] Murata et al. showed that CAE was superior to the proper orthogonal decomposition methods with regard to the extraction of fluid flow around a cylinder via dimension reduction.[14]

Akin to most of the machine learning methods, the CNNs, however, rely essentially on the availability of big data as the input for training, in order to extract the most important characteristics of the high-dimensional and complex nonlinear fluid flows. Direct numerical simulation (DNS) can be used to generate big datasets of a fluid flow at the cost of fine time steps. But the DNS data are noise-free and lack of experimental validation at fine time steps. PIV experiments, on the other hand, provide the direct measurements of the fluid flows. However, as discussed above, PIV can only offer a small dataset due to the high cost for both high temporal resolutions and spatial resolutions in the measurements.

In addition, in order to broaden the adaptability of the model in a wide variety of flow conditions, it is common to add some extra information into the CNNs, i.e., the flow conditions and particle properties based on the noiseless numerical simulation data, as the inputs of CNNs pipeline such that a relatively smaller dataset is sufficient to capture the features of the fluid flows for various flow conditions.[20,28,29] For example, Zhang et al. added Mach numbers, *Re* and attack angles for fluid flow around a particle into the CNNs structure to broaden the adaptability of the model under a wide variety of flow conditions.[28] However, in practice, it is not always possible to obtain an accurate prior information such as flow conditions and particle properties in practical PIV measurements with noised data. Incorporating additional information as inputs to the CNNs pipelines is not always reliable in dealing with noised data in PIV measurements.

According to the previous literature,[20,30] the typical convolutional neural network, CAE, was adopted and could have good performances on flow reconstructions. However, for noisy small PIV experimental datasets, it is hard to reconstruct flow fields which may be due to the common loss of details of the flow field during the encoding process of CAE. And it is found that the residual network (*re*CAE) and skip-connection network (*sc*CAE) can solve this problem to a certain extent. Hence, in this work, we systematically compared the performances of these three networks in detail (CAE, *re*CAE and *sc*CAE) for reconstructing and predicting flow fields based on small PIV experimental data with noises and study the influence of different hyperparameters on the performances. Eventually, a suitable network of *sc*CAE was selected to accurately reconstruct the time-resolved flow field with noisy small data obtained by PIV measurements based on dimension reduction and feature capturing for different *Re*, bluff body shapes and time-evolution features. In addition, the network also has a good performance on flow prediction for different *Re*, bluff body shapes and temporal evolution features.

This article is organized as follows: The description of experimental apparatus and data processing is provided in Section 2 to clarify the source of data. The principle of convolutional neural networks, autoencoder network, training algorithm and dataset is given in Section 3 to illuminate the detailed operations of machine learning methods. In Section 4, the effect of the latent vector size was first investigated to optimize the *sc*CAE model. Then, the loss function was used to evaluate the stability and robustness of the model. The performances in capturing spatiotemporal features of the flow fields of *sc*CAE were further quantified in terms of their reconstructed flow fields for extrapolated *Re* of 400, 1000, and 1400, which had a better performance than those of CAE and *re*CAE. Both flow around a sphere and a cube were evaluated to test the robustness of the *sc*CAE model for different shapes. Furthermore, predictions of the flow fields based on low-dimensional vectors, which including the flow field physics for a sphere and/or a cube were performed respectively to further test performances of feature extractions.

https://doi.org/10.1021/acs.iecr.1c04704
Ind. Eng. Chem. Res. 2022, 61, 8504−8519

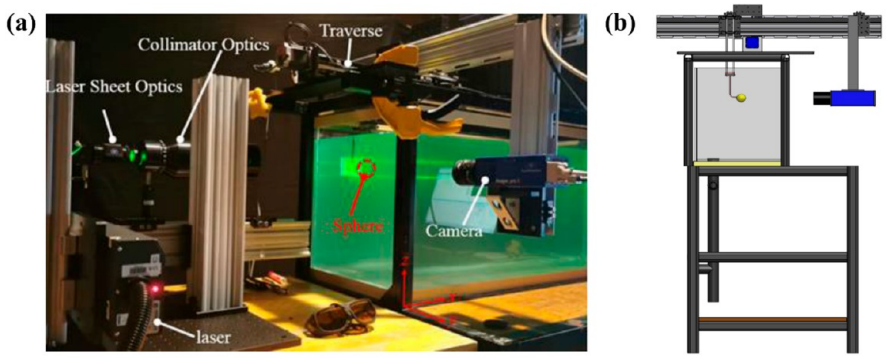

Figure 1. (a) PIV experimental setup and (b) its sideview.

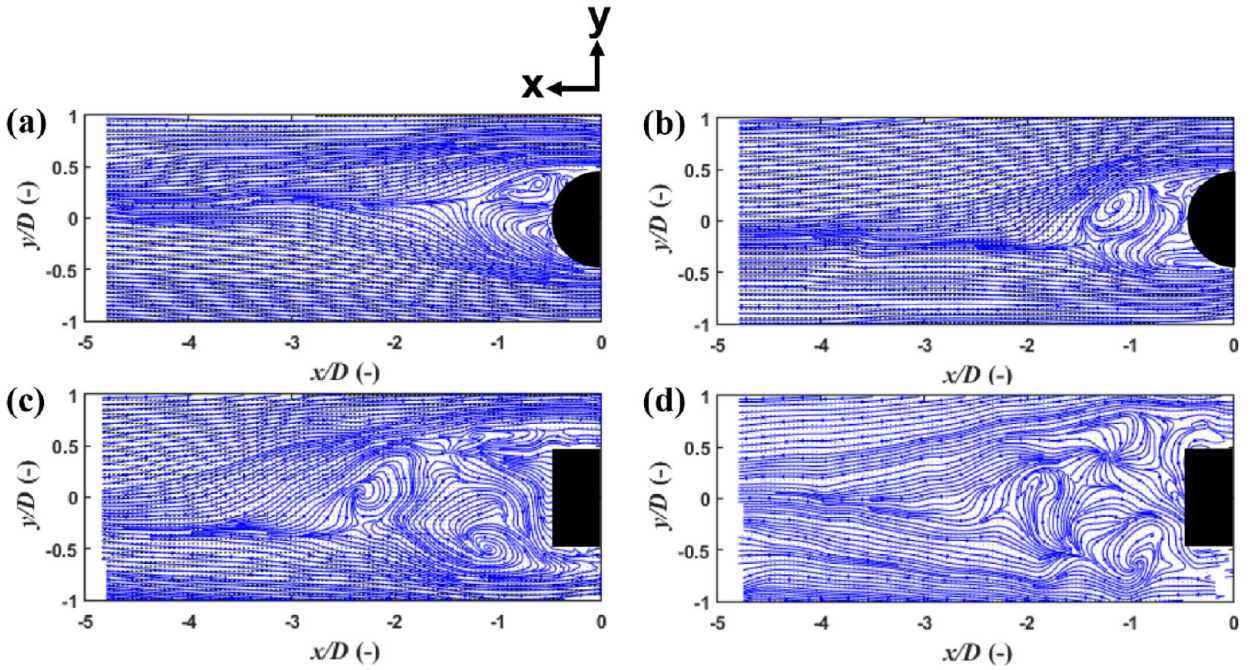

Figure 2. Typical flow fields as inputs for training and validation. (a) and (b) are instantaneous flow fields for flow around a sphere at *Re* = 600 and *Re* = 1200, respectively; (c) and (d) are instantaneous flow fields for flow around a cube at *Re* = 600 and *Re* = 1200, respectively. (The blank in the left of each figure represents that the flow fields in this area were not measured).

2. EXPERIMENTS

2.1. Experimental Apparatus. All inputs in the *sc*CAE model were vector fields obtained from our PIV experiments. As shown in Figure 1a, a two-dimensional PIV setup was used to capture the instantaneous flow fields. A double-pulsed Nd:YAG laser source (Model Solo III-15z, New Wave) with a nominal maximum power of 50 mJ/pulse was used to illuminate the flow. The wavelength of the laser was 532 nm, and a laser sheet optics and a collimator optics were used to convert the laser beam into a relatively narrow laser sheet. A 14-bit double-frame CCD camera (Model Imager Pro X 4M, LaVision) with 2112 × 2072 pixel resolutions was synchronized to the laser to capture images of fluid flows and a 50 mm SLR camera lens (Nikkor) was used. Hollow glass spheres of size 18 μm with a density of 0.6 g/cc (Potters Industries) were used as seeding particles. The acquisition frequency of the camera for 2D-2C PIV vector fields was double-frame rate of 5.05 Hz, which was sufficient to track the dominant flow structures in this work. PIV measurements were conducted in a water tank with a large test section of 400 mm × 500 mm × 1200 mm, which could ensure the elimination of side wall effects in all *X*, *Y*, and *Z* directions (as shown in Figure 1b). The model particle was connected to a traverse (VELMEX. Inc.) moving in the horizontal direction. Two different model particles, i.e., a solid sphere and a solid cube with the same characteristic length of 30 mm, were used. The traverse controlled with a controller could move with a constant velocity to provide a certain *Re*. The laser sheet was adjusted to pass through the central plane of the model particle (sphere and/or cube). Fields of views of the camera were extended to ∼5 times the characteristic length of a single model particle to ensure that wake characteristics in freestream directions could be sufficiently captured. Time-dependent flow fields were recorded from the initial time of wake formations.

The commercial software (Davis 8.2, LaVision GmbH) was used to calculate vector fields from raw fluid pictures (images of seeding particles) and the overall data preparation procedures were as follows. First, the collected raw images of the seeded flow fields were enhanced by sliding minimum subtraction and min-max filter for intensity normalization.

https://doi.org/10.1021/acs.iecr.1c04704
Ind. Eng. Chem. Res. 2022, 61, 8504−8519

Then, cross-correlation analysis was used to calculate the vector fields from raw pictures with multiple passes on the window sizes. The interrogation window of 64 × 64 pixels with 50% overlap was selected for the first pass and the interrogation window with the size of 32 × 32 pixels with 50% overlap was selected for the second pass.

2.2. Train and Test Dataset. The two-dimensional vector fields for flow around the sphere and cube were obtained for moderate Reynolds numbers (Re = 400, 600, 800, 1000, 1200 and 1400). Some samples of vector fields are shown in Figure 2. Here, the flow velocity component along the freestream direction x in vector fields was denoted as U and the corresponding component along the vertical direction y was defined as V. The frames and properties of all PIV data for train, validation and test datasets are summarized in Table 1.

Table 1. Summary of Frames and Properties of All PIV Data

shapes of particle	Reynolds number, Re	number of frames
Train and Validation Datasets		
sphere	600	258
	800	197
	1200	129
cube	600	253
	800	190
	1200	126
Test Datasets		
sphere	400	392
	1000	154
	1400	113
cube	400	380
	1000	150
	1400	111

The datasets for flow fields at Re = 600, 800 and 1200 were employed as the input to train the model and capture the underlying features of spatiotemporal evolutions of the fluid flow around a single particle. Each input data set was split randomly into a train dataset (70% of the data in the input dataset) and a validation dataset (30% of the data in the input dataset). All snapshots were recorded as single images with a spatial resolution of 128 × 128.

Typical instantaneous flow fields at Re = 600 and 1200 for flow around a sphere and/or a cube are shown in Figure 2. As can be seen, the fluid flow around a sphere is different from that of a cube even at the same Re. For fluid flow around a cube, the intense wakes can be observed, with more eddies and shedding appearing at the downstream of the cube. Meanwhile, the size of wakes including both wake length and wake width in the fluid flows around both the sphere and cube varies with Re. Thus, in order to test the extrapolated performance of our proposed *sc*CAE in dimension reduction and characteristics capturing for different shapes, different Re and different time-evolution information, the datasets of time-resolved instantaneous flow fields for three extrapolated Re, i.e., 400, 1000, and 1400 for both flow around the sphere and the cube were used as test datasets, in which the quantitative comparisons of highly nonlinear flow fields reconstructed and predicted based on the low-dimensional latent vectors with the ground truth flow fields were provided.

3. METHODOLOGY

3.1. Convolutional Neural Networks (CNNs). Typical CNNs consist of three operations: the convolution, pooling and upsampling, as shown in Figure 3. For the input $X \in R^{M\times N}$, with a filters W with kernel size of $\in R^{m\times n}$, the convolutional results Y can be obtained by

$$Y_{ij} = \sum_{u=1}^{m}\sum_{v=1}^{n} W_{uv}\cdot X_{i-u+1,j-v+1} \tag{1}$$

Based on eq 1, it can be found that different kernel sizes can extract different features, resulting in different convolutional layers. In Figure 3a, the input is $X \in R^{5\times5}$, the filter is $W \in R^{3\times3}$ and the obtained is $Y \in R^{3\times3}$. The pooling layer aims to obtain spatially invariant features by reducing the resolution of the features. As shown in Figure 3b, the data can be compressed by $(1/P)^2$ times with max pooling which supposes that the maximum value represents a region with a pool size of $P \times P$. By combining the convolutional and pooling layers, it is possible to reduce the dimensions while retaining the features of the input data. Similarly, the upsampling is used to enlarge the data by copying, as shown in Figure 3c.

3.2. Autoencoder Network. As discussed above, the challenge in dealing with the small datasets obtained in PIV measurements is the data compression and dimension reduction. CAE has shown good performances of data compression and dimension reduction in the images of fluid flows.[14,26] However, because of the inevitable loss of the details of inputs in the pooling layers in CAE, the original images

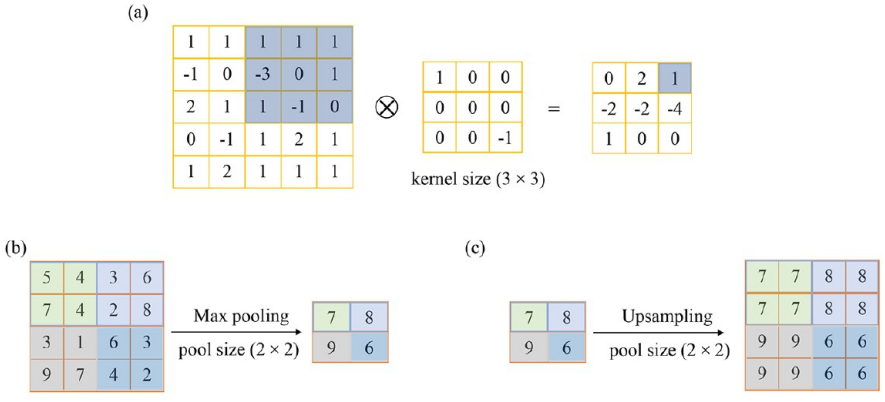

Figure 3. Operations of the CNN: (a) convolution, (b) max pooling and (c) upsampling.

https://doi.org/10.1021/acs.iecr.1c04704
Ind. Eng. Chem. Res. 2022, 61, 8504−8519

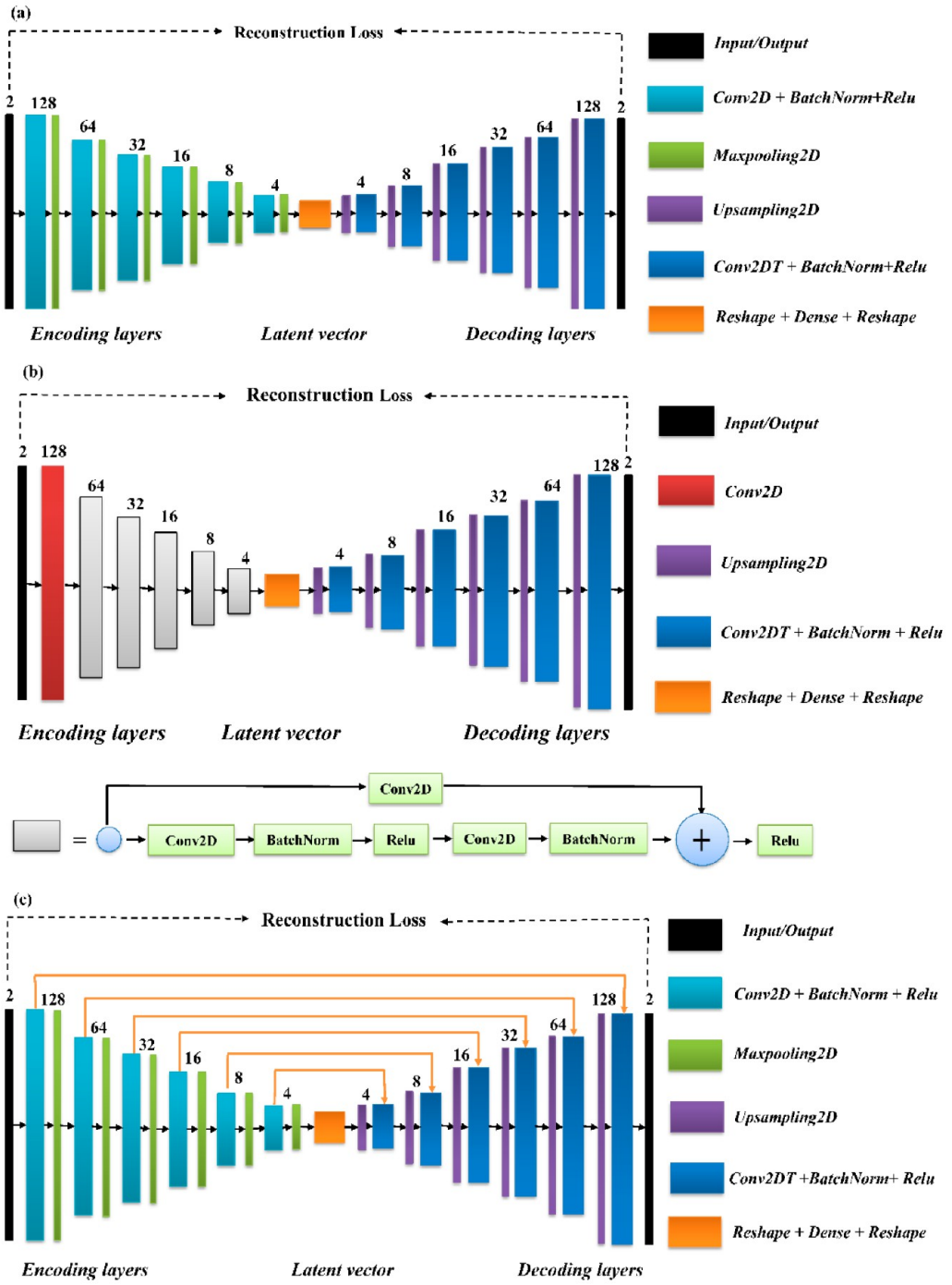

Figure 4. Architecture networks implemented in this work: (a) CAE, (b) *re*CAE (each gray block is a convolutional residual block with the normalization) and (c) *sc*CAE (the black arrows denote convolutional layers, while the orange arrows indicate skip connections).

cannot be completely recovered from the latent vector, especially for the small train dataset. It has been argued that a better performance could be obtained by deepening the network, i.e., increase the number of layers, which, however, introduces other issues such as gradients vanishing and network degradation.[31] Later on, the residual CAE (*re*CAE) was proposed to improve the performance of the deeper CNNs.[32,33] Motivated by the *re*CAE, the skip connections have been further developed in computational image processing in order to restore the spatial information lost during the down-sampling. The skip connections approach can recover the images by passing image details forwardly on the one hand, and achieve local minimum by passing gradient backwardly on the other hand.[34] U-Net, for example, incorporated the long skip connections[35] and was successfully applied to predict pressure fields across different airfoils and flow conditions.[36] In this work, by modifying the convolutional, deconvolutional layers and other hyper-parameters used in U-net, a long skip connection based on CAE (*sc*CAE) is proposed for dimension reduction in fluid flow around a single particle using a small PIV dataset. For comparison, both CAE and residual CAE are also presented.

https://doi.org/10.1021/acs.iecr.1c04704
Ind. Eng. Chem. Res. 2022, 61, 8504−8519

3.2.1. CAE. The architecture of CAE, as illustrated in Figure 4a, consists of two parts, namely, the encoder part ($\mathcal{F}_e$) and decoder part ($\mathcal{F}_d$). The encoder part is composed of multiple encoding layers and can encode the input q into a lower dimensional space, which is defined as the latent vector $\tilde{q}$. Similarly, the decoder part is also composed of multiple decoding layers, which can decode the latent vector to a higher dimensional space, q_{deco}. If q_{deco} is identical to q, the CAE works perfectly and the dimensions can be successfully reduced while the latent vector includes almost all information of the input. Mathematically, the procedure of CAE can be expressed as eq 2:[29]

$$\tilde{q} = \mathcal{F}_e(q) q_{deco} \approx \mathcal{F}_d(\tilde{q}) \tag{2}$$

As depicted in Figure 4a, the encoder part has six blocks, with each consisting of a convolution layer, a batch normalization layer, an activation function and a pooling layer. The convolutional layer is the key of CAE, which can extract the main features of the input using a certain number of filters. In this work, the filter size was set as 3 × 3 for all layers. To accelerate the learning and avoid the overfitting, the batch normalization,[37] which normalized the output of each unit based on the mean and variance, was adopted. Considering the fast converge speed without the complicated mathematics as well as the function of stable weight update, the nonlinear activation function or rectified linear unit (ReLu), was normally used.[38] For pooling layer, two pooling schemes, i.e., average pooling and max pooling, were commonly used.[39] In current work, max pooling was chosen in which the pooling was achieved by selecting the maximum value from the feature maps covered by the corresponding filter (Figure 3b). The decoder part was similar to the encoder part and also consisted of six blocks, with each block including the upsampling layer (Upsampling2D), the transposed convolutional layer (Conv2DT), the BarchNorm layer and the ReLu layer, in order. The unsampling layer was utilized to gradually expand the size of dimensionality and transform the data in the lower-dimensional space to that in the higher-dimensional space.

3.2.2. Residual CAE (reCAE). In residual network, the residual of unit l must be calculated by eqs 3 and 4:[40]

$$y_l = x_l + F(x_l, w_l) \tag{3}$$

$$x_{l+1} = f(y_l) \tag{4}$$

where F is the residual function, f is the ReLu function, and x_l and x_{l+1} are input and output of the lth unit, respectively. As shown in Figure 4b, each of the residual blocks (gray block) consists of a convolutional layer, a batch normalization layer, an activation function, a convolutional layer, a batch normalization layer and a shortcut connection. The encoder part of the *re*CAE differs from that in the CAE. In the *re*CAE, the image size was progressively down-sampled by a factor of 2 with stridden convolutions instead of the max pooling layer. This allows the network to increasingly extract more abstract information at a larger scale with the growing number of feature map channels.[41] After a series of successive stridden convolutions, the size of feature maps becomes smaller and smaller compared to that of the input images, and eventually the latent vector can be obtained. The input first goes through an up-sampling layer to be reshaped to a tensor of size 128 × 128 × 128, then five residual blocks are used to derive the latent vector. The decoder part comprises six blocks, which is same as the decoder in the CAE network, as shown in Figure 4a.

3.2.3. Skip Connections CAE (scCAE). In the *sc*CAE developed in this work, the long skip connections were implemented and the connections were not cropped before being copied. By doing so, the entire information on inputs in the decoder layers was preserved, in which a prior addition of parameters reflecting key features was not desired. As shown in Figure 4c, the *sc*CAE proposed in this work consists of a series of symmetric encoding layers and decoding layers. The encoding layers act as the feature extractor and the decoding layers decode the latent vector to restore the image details. And the skip connections are added from the convolutional layers to their corresponding mirrored deconvolutional layers. Using the skip connections, the passed convolutional feature maps are summed to the deconvolutional feature maps by elements.

As shown in Figure 4, for all three CAEs, the raw inputs used in this work were vector fields obtained from PIV experiments, which could be expressed as a 3D matrix of size 128 × 128 × 2. Then, a 3× 3 convolution layer was performed with a fixed map channel [128, 64, 32, 16, 8, 4], respectively. The decoder could be used to reconstruct the vector fields from the latent vector, which represented the most important features of the fluid flows. In the decoder part, another 6 symmetric layers were used, with the kernel size of 3 × 3 and the feature map channel of [4, 8, 16, 32, 64, 128]. The eventual output would have the same size as that of the original input using a convolution with 2 channels and a sigmoid function.

3.3. Training Algorithm. To achieve the satisfactory performance, it normally needs data preprocessing. In this work, a common min−max normalization was implemented by eq 5:

$$x' = \frac{(x - x_{min})}{(x_{max} - x_{min})} \tag{5}$$

where x' is the normalized data, and x_{max} and x_{min} are, respectively, the maximal and minimal values. The model performance was evaluated against MSE defined in eq 6:

$$\text{MSE} = \frac{1}{n}\sum_{t=1}^{n}(b_t - p_t)^2 \tag{6}$$

where n is the size of the sample, p is the predicted value and b is the observed value. The loss function MSE, as defined in eq 6, was minimized during the training process to obtain the optimal parameters. The backpropagation method which involves the calculation of the gradients of loss function, with respect to learnable parameters was implemented for training.[42] The adaptive moment estimation (Adam) was employed as the optimization algorithm.[43] The total epoch of 1000 was assumed and the early stopping was implemented to avoid overfitting. The training process had been executed in sequence for each time step unless the maximum epoch (1000) or early stop (200) was first reached. The in-house code for our proposed method has been written based on the Tensorflow 2.4.3 and Keras 2.6.0 libraries on Python 3.8.

4. RESULTS AND DISCUSSIONS

4.1. Size of the Latent Vector. In this section, the influence of latent vector size in *sc*CAE was discussed. It has been previously shown that the characteristics of the high-dimensional flow fields could be well-captured and recon-

https://doi.org/10.1021/acs.iecr.1c04704
Ind. Eng. Chem. Res. 2022, 61, 8504−8519

structed using CAE based on the latent vector obtained by dimension reduction.[29,44] Murata et al. further showed that the periodic change of the latent vector could reflect the vortex shedding.[14] Therefore, the latent vector is critical in capturing the characteristics of high-dimensional and nonlinear flow fields. Thus, the dependence of RMSE on the latent vector size in *sc*CAE was investigated. Four latent vector sizes, i.e., 2, 4, 8 and 16, were examined. Normally a smaller latent vector size allows the lower computational cost for *sc*CAE. However, if the latent vector size is too small, some key features might be lost. Our results suggest that the lowest RMSE was achieved with the latent vector size of 4 for different *Re*. Figure 5 shows the

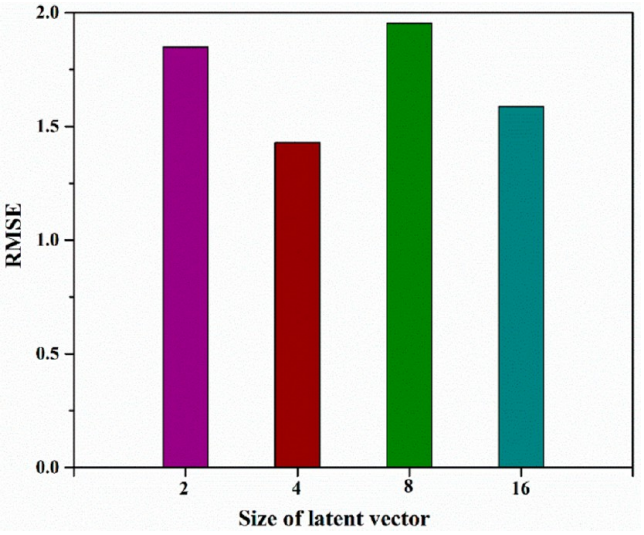

Figure 5. Effect of the latent vector size on RMSE in *sc*CAE for fluid flow around a sphere at *Re* = 600.

typical results of RMSE for fluid flows around a sphere at *Re* = 600. Thus, in this work, the latent vector size was set as 4 and the corresponding compression ratio, which was defined as the ratio between the dimension of input and that of the latent vector, was 1.2×10^{-4}.

4.2. Training of the Models. In order to test the performance of the proposed *sc*CAE in dimension reduction and flow characteristics capturing, the reconstructions of flow fields based on the latent vector were conducted. For comparison, the reconstruction performances of CAE and *re*CAE were also evaluated. Note that the loss is an important indicator for assessing whether the steady and robust results could be achieved, so the loss for the train and validation datasets, as a function of the epoch for CAE, *re*CAE, and *sc*CAE, were performed first, as shown in Figure 6. Here, an epoch refers to the process of sending the data into the network to complete a forward calculation and back-propagation. The training loss, which was represented by the mean square error (MSE) between vector fields reconstructed and those obtained by the corresponding PIV experimental datasets, was used to evaluate the convergence during the training process. And the validation loss was used to verify the ability of generalization and decide whether the training was needed to be stopped in advance.

For CAE, as shown in Figure 6a, the loss curve first demonstrates a spike, which is as high as 0.035, and then gradually approaches ~0.0018 with small fluctuations. The loss for *re*CAE starts at 0.038, moves downward during training and finally oscillates near 0.0016. The loss of *sc*CAE shows the best performance: the training loss converges very quickly and barely descends after 50 epochs, eventually remaining at 0.00014. This indicates that the skip connections in *sc*CAE could accelerate the convergence during the learning process. The loss on the validation dataset was also computed and the results are depicted in Figure 6b. In this case, the final loss of CAE is 0.002, oscillating near 0.0018 and 0.0023 after 600 epochs. The final loss of *re*CAE is 0.0018, oscillating near 0.0017 and 0.0022 after 600 epochs. The final loss of *sc*CAE is 0.00019, which is one order of magnitude smaller than that of others two models, which again emphasizes the generality and robustness of *sc*CAE. In other words, both the training and validation loss in *sc*CAE can converge with no overfitting, which indicates that our proposed model could achieve steady and robust reconstruction results after proper training.

For train and validation datasets for *Re* = 600, 800 and 1200, the error metrics RMSE for the vector fields reconstructed for flow around a sphere and a cube are shown in Figure 7. As can be seen, the RMSEs of both *U* and *V* obtained by *sc*CAE are much lower than those of CAE and *re*CAE for all cases, illustrating the proposed *sc*CAE has better performances on reconstruction of the time-series flow fields for different *Re* and

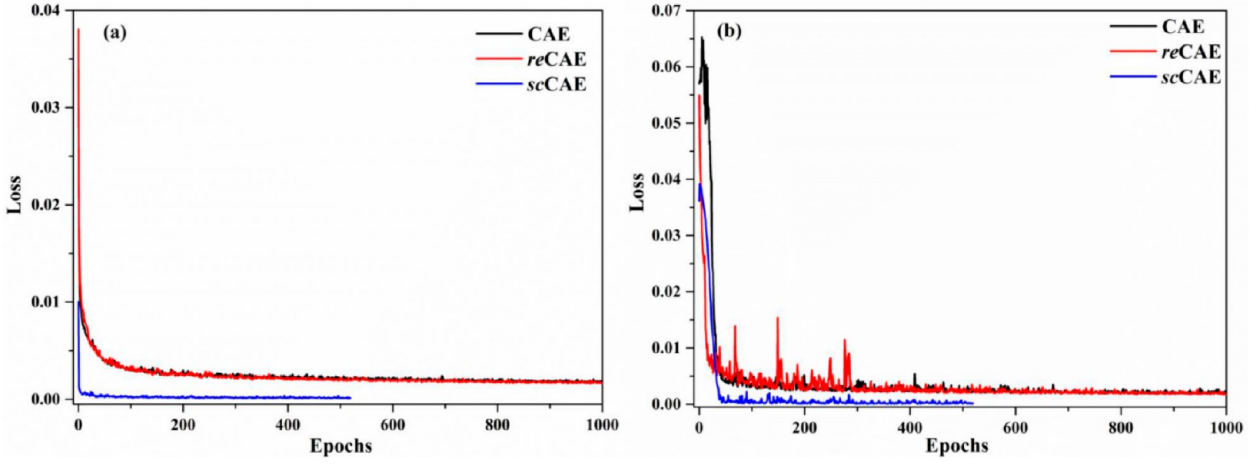

Figure 6. Loss on the train datasets (a) and validation datasets (b) for different models.

https://doi.org/10.1021/acs.iecr.1c04704
Ind. Eng. Chem. Res. 2022, 61, 8504−8519

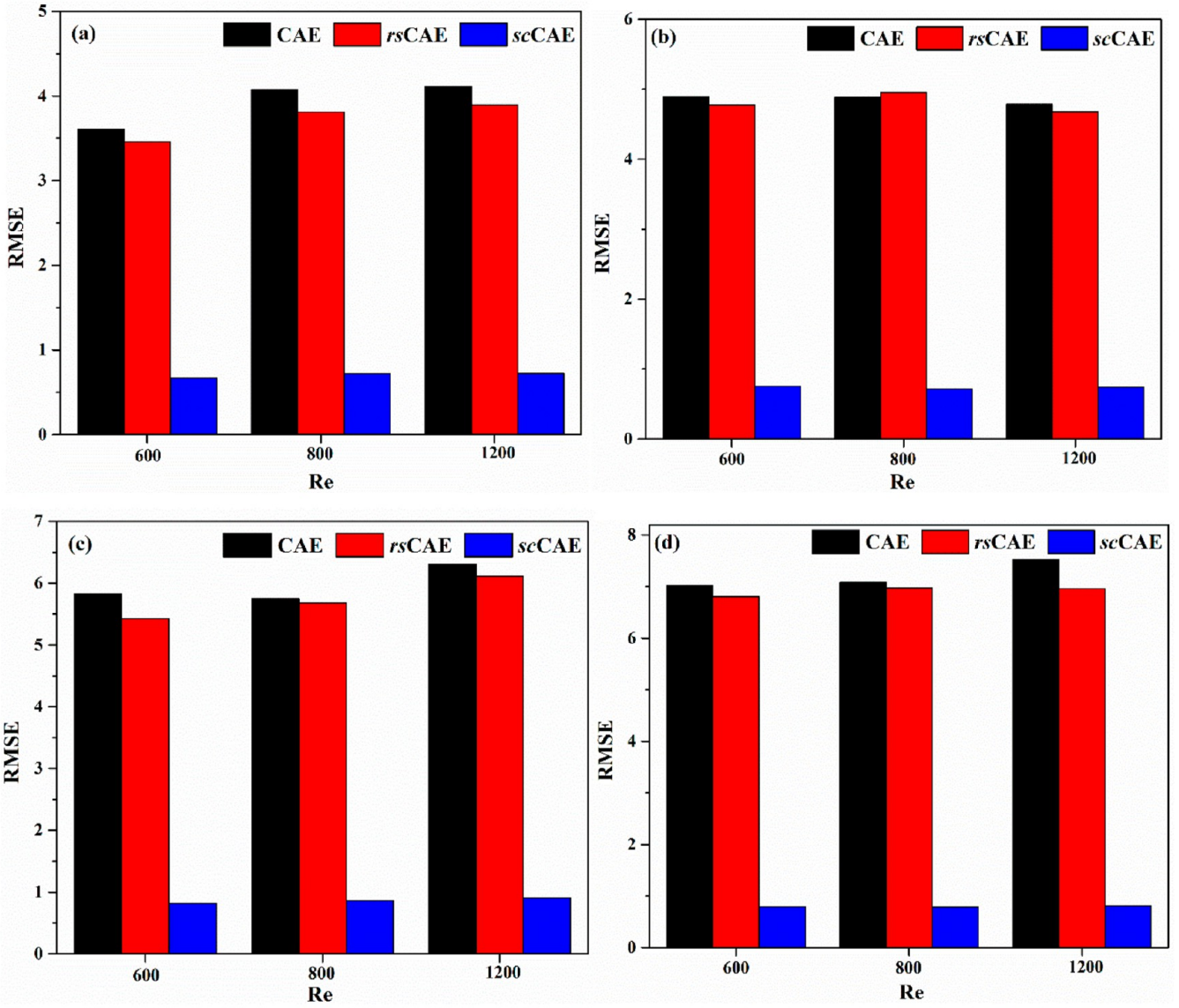

Figure 7. Root mean square error (RMSE) values of U ((a) sphere and (c) cube) and V ((b) sphere and (d) cube) for different training Re of different models.

geometrical shapes. So, the proposed *sc*CAE can well capture the underlying flow characteristics based on a small input dataset of PIV experiments.

4.3. Flow around a Sphere. The performances of spatiotemporal feature extractions for CAE, *re*CAE and *sc*CAE were first investigated in terms of their performances in reconstructing flow fields around a sphere for extrapolated Re of 400, 1000 and 1400 and time-evolution information. In this section, the time-series PIV vector fields from the initial instance of wake formations to the fully developed states, covering various status of the high dimensional and nonlinear characteristics in flow fields, for the sphere were reconstructed for each Re.

Instantaneous vector fields obtained directly from the original PIV measurements were compared with the corresponding reconstructed vector fields. Figure 8 shows typical snapshots of instantaneous vector fields of frame 90 at Re = 400 and Re = 1400 obtained by different models. As can be seen, flow fields reconstructed by CAE (Figures 8b, 8f, 8j and 8n) and *re*CAE (Figures 8c, 8g, 8k and 8o) included the dominant flow structures near the rear region of the sphere for U, but missed detailed flow patterns appearing far away from the sphere for U. And it failed to capture flow features for V for all regions at Re = 400. Meantime, vector fields reconstructed using the *sc*CAE (Figures 8d, 8h, 8l and 8p) can well recover the results of ground truth obtained directly from PIV datasets (Figures 8a, 8e, 8i and 8m). Furthermore, a close check shows that all eddies and flow details far from the sphere were also satisfactorily captured by the *sc*CAE. Thus, the *sc*CAE proposed in this work was able to reconstruct vector fields around a single sphere at moderate Re using limited PIV experimental data as inputs. In addition, the streamlines reconstructed by the *sc*CAE, as well as the original streamlines obtained by PIV experiments for instantaneous flow field of frame 90 for flow around a sphere at Re = 1400 are shown in Figure 9, which shows a pretty good reconstruction performance on the capture of flow details.

Then, the component velocity U and V varying with time at specified positions for flow around a single sphere for various Re were quantitatively assessed. Typical results at two positions

https://doi.org/10.1021/acs.iecr.1c04704
Ind. Eng. Chem. Res. 2022, 61, 8504−8519

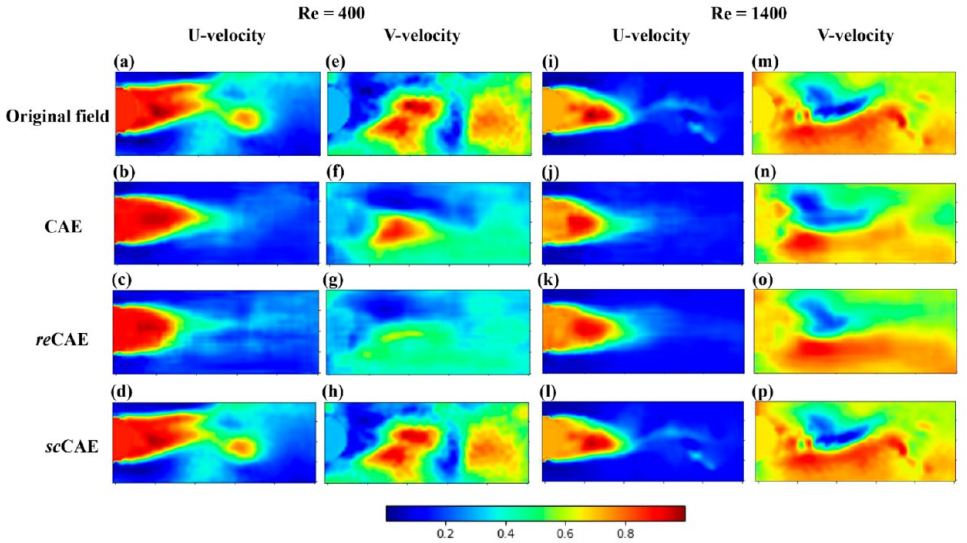

Figure 8. Typical snapshots of vector fields around a sphere for original fields and those reconstructed by CAE, *re*CAE and *sc*CAE: (a–d) *U*-velocity at Re = 400, (e–h) *V*-velocity at Re = 400, (i–l) *U*-velocity at Re = 1400, (m–p) *V*-velocity at Re = 1400.

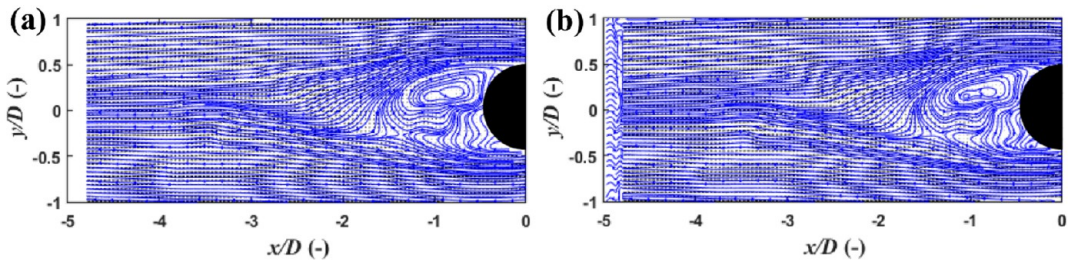

Figure 9. Typical snapshots of the streamlines around a sphere at Re = 1400 for frame 90: (a) PIV experimental results, (b) reconstructed by *sc*CAE. (The blank in the left figure indicates that the flow fields in this area were not measured.)

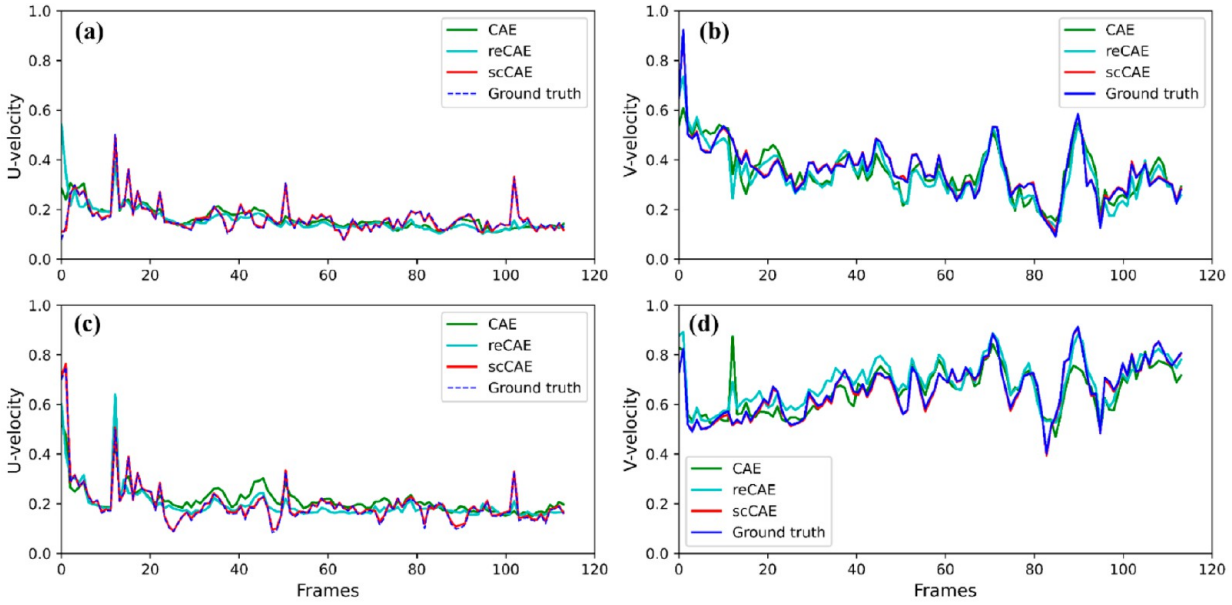

Figure 10. Comparisons of time series of flow velocity components at Re = 1400 between the three models reconstruction results and the ground truth PIV measurement results: (a) U at $(X/d = 1.5, Y = 0)$, (b) V at $(X/d = 1.5, Y = 0)$, (c) U at $(X/d = 2.5, Y = 0)$, (d) V at $(X/d = 2.5, Y = 0)$.

$(X/d = 1.5, Y = 0)$ and $(X/d = 2.5, Y = 0)$ for Re = 1400 are shown in Figure 10. Here, X is the distance from the sphere center to the monitoring point and d is the diameter of the sphere. As can be seen, the time series of the components U and V reconstructed by *sc*CAE for both $(X/d = 1.5, Y = 0)$ and $(X/d = 2.5, Y = 0)$ well match that obtained directly from the ground truth data set measured by PIV. This means that *sc*CAE can well capture the time-evolution flow structures in

https://doi.org/10.1021/acs.iecr.1c04704
Ind. Eng. Chem. Res. 2022, 61, 8504–8519

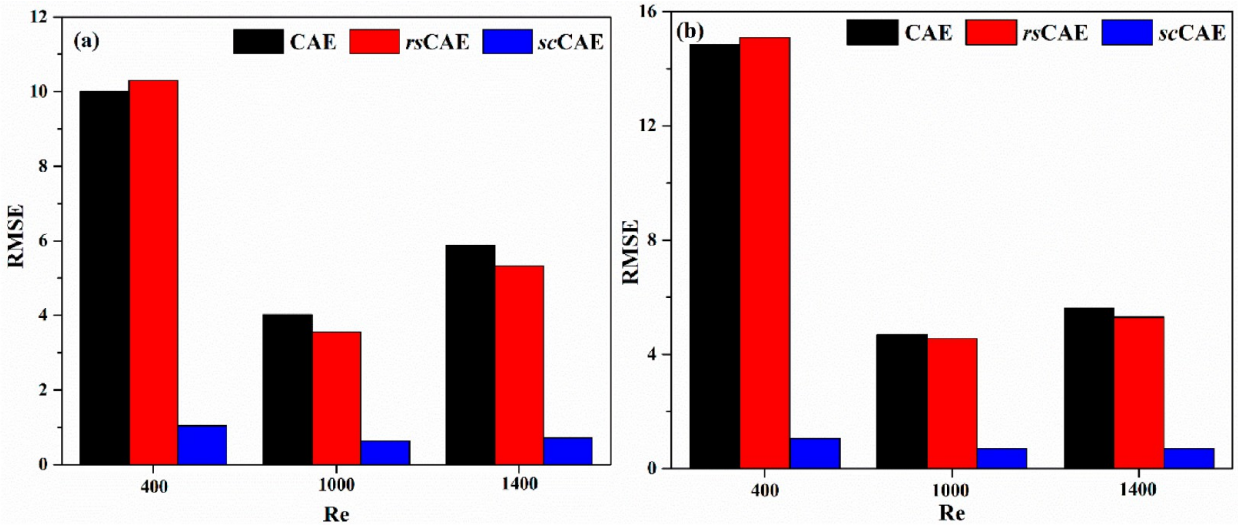

Figure 11. RMSE of (a) *U* and (b) *V* for different testing *Re* of different models.

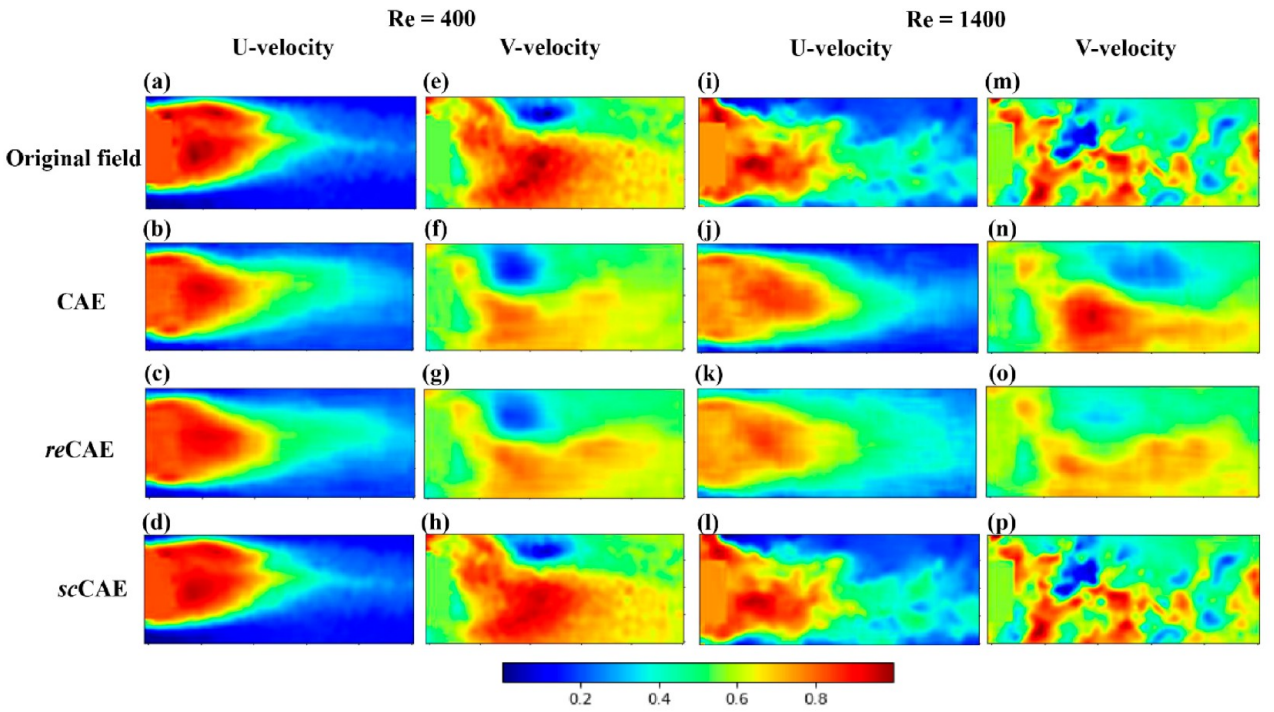

Figure 12. Typical snapshots of vector fields around a cube for original fields and those reconstructed by CAE, *re*CAE and *sc*CAE: (a−d) *U*-velocity at *Re* = 400, (e−h) *V*-velocity at *Re* = 400, (i−l) *U*-velocity at *Re* = 1400, (m−p) *V*-velocity at *Re* = 1400.

the whole flow fields. Besides, the *sc*CAE manifests much better performances than CAE and *re*CAE in reconstructing flow fields because the other two models show considerable deviations from the PIV results. Thus, *sc*CAE can not only capture the evolution process with time of the flow fields around a sphere, which demonstrated complex vortex phenomena, but also quantitatively reproduce the spatial velocity distributions for the whole flow fields.

Error metrics RMSE for vector fields reconstructed using different models under test datasets *Re* = 400, 1000, and 1400 were evaluated in Figure 11. As can be seen, RMSEs of both *U* and *V* obtained by *sc*CAE are much lower than those of CAE and *re*CAE for all extrapolated *Re*, indicating the proposed *sc*CAE was robust in reconstructing the time-series flow fields for extrapolated *Re*. In addition, as shown in Figure 11, low RMSE values of *U* and *V* obtained by *sc*CAE for the test datasets reveal the proposed *sc*CAE has a good extrapolation performance on reconstruction the spatiotemporal evolution of moderate-*Re* flows around a sphere.

4.4. Flow around a Cube. In this section, the proposed *sc*CAE was further tested by reconstructing flow fields around a cube using limited PIV experimental data. For comparisons, the performances of flow field reconstructions for CAE and *re*CAE were also assessed.

Our results show that the vector fields reconstructed by *sc*CAE were in good accordance with the results obtained via PIV measurements for extrapolated *Re* = 400, 1000, and 1400. Figure 12 shows the typical results of reconstructed vector

https://doi.org/10.1021/acs.iecr.1c04704
Ind. Eng. Chem. Res. 2022, 61, 8504−8519

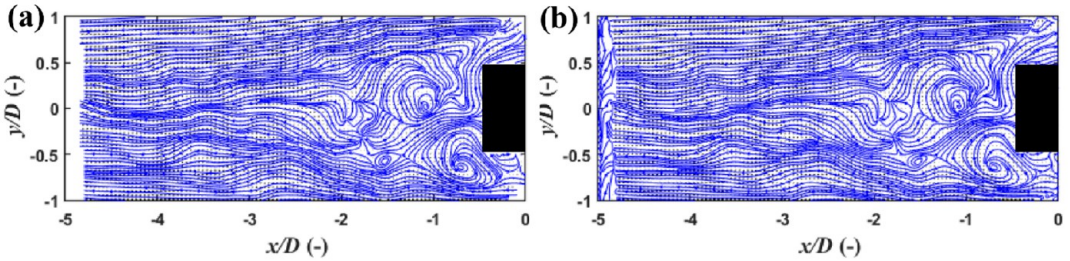

Figure 13. Typical snapshots of the streamlines around a cube at Re = 1400 for frame 90: (a) PIV experimental results, (b) reconstructed by *sc*CAE. (The blank in the left figure indicates that the flow fields in this area were not measured.)

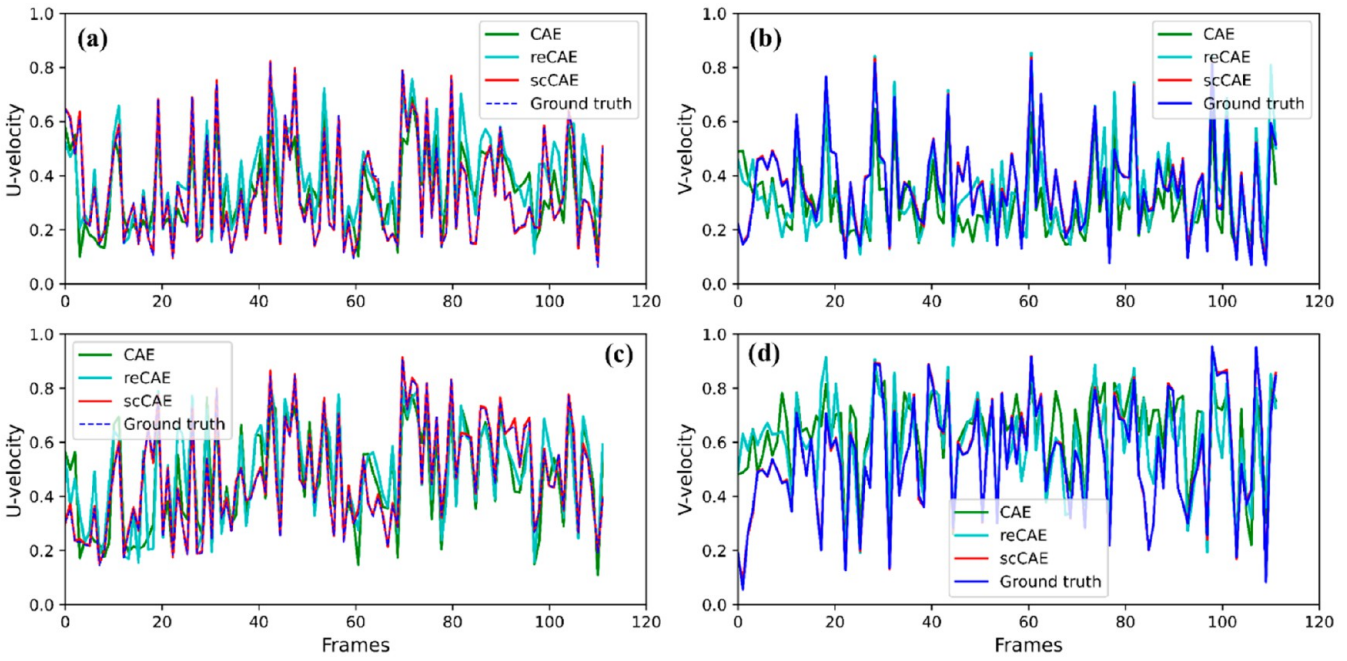

Figure 14. Comparisons of time series of flow velocity components at Re = 1400 between the three models reconstruction results and the ground truth PIV measurement results: (a) U at (X/d = 1.5, Y = 0), (b) V at (X/d = 1.5, Y = 0), (c) U at (X/d = 2.5, Y = 0), (d) V at (X/d = 2.5, Y = 0).

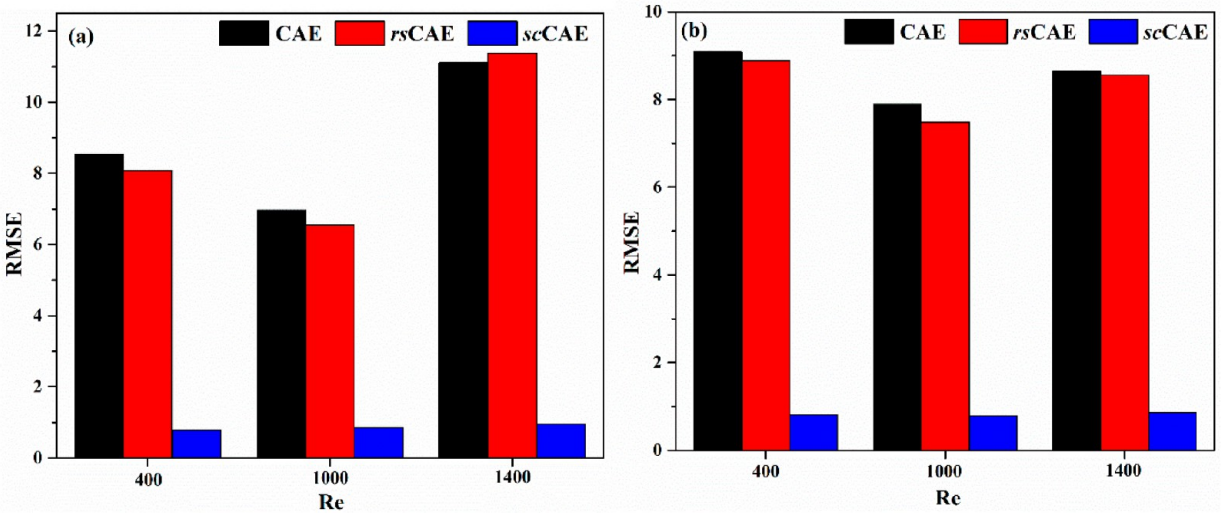

Figure 15. RMSE of (a) U and (b) V for different testing Re of different models.

fields at Re = 400 and Re = 1400 respectively. The original PIV datasets were taken from the frame 90 for all Re in Figure 12. As can be seen, the components U and V reconstructed using *sc*CAE (Figures 12d, 12h, 12l, and 12p) are consistent with U and V of the ground truth based on PIV experimental data (Figures. 12a, 12e, 12i, and 12m), indicating that the *sc*CAE can capture the details of flow fields around the cube. Flow fields reconstructed by CAE (Figures 12b, 12f, 12j, and 12n)

https://doi.org/10.1021/acs.iecr.1c04704
Ind. Eng. Chem. Res. 2022, 61, 8504−8519

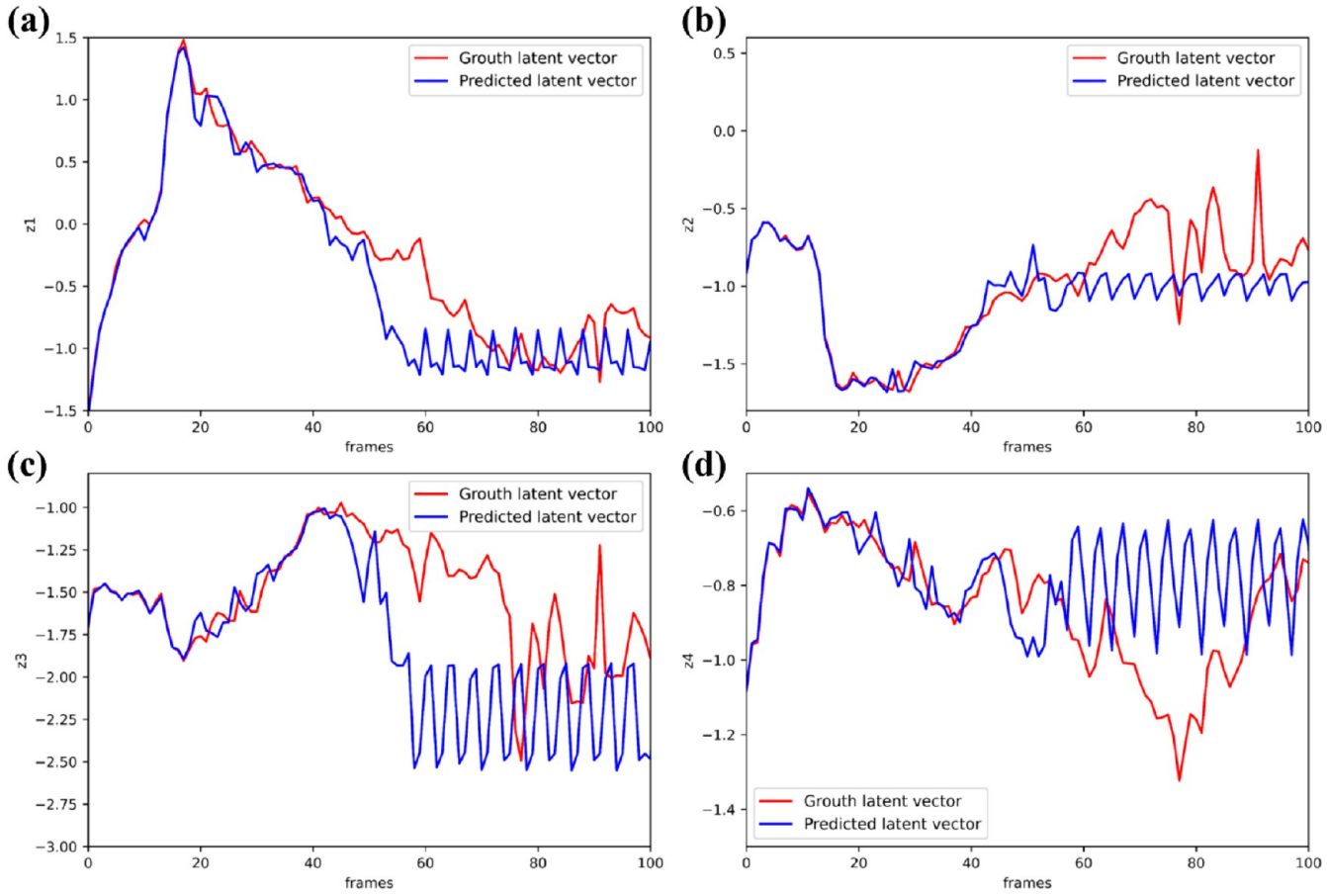

Figure 16. Comparisons of temporal evolutions along the four latent components between the original data (red) and the *sc*CAE prediction (blue) for flow around a sphere at $Re = 600$: (a) the first latent component $z1$, (b) the second latent component $z2$, (c) the third latent component $z3$, (d) the fourth latent component $z4$.

and *re*CAE (Figures 12c, 12g, 12k, and 12o), however, only capture the dominant flow features for *U*, and fail to obtain flow features for V. It was also provided the typical streamlines reconstructed by the *sc*CAE as well as the original streamlines obtained by PIV experiments for instantaneous flow field around a cube, as shown in Figure 13. As can be seen, *sc*CAE can reconstruct almost all the details, such as wakes behind the cube.

The typical time-series *U* and *V* reconstructed for $Re = 1400$ at two monitoring points $(X/d = 1.5, Y = 0)$ and $(X/d = 2.5, Y = 0)$ are respectively plotted in Figure 14. As it was known, wakes in the fluid flow around a cube are significantly more intense with more eddies and shedding appearing downstream than those of the sphere. So, the flow velocities at certain points show much more complex fluctuations than those of the sphere. As can be seen in Figure 14, time series of *U* and *V* reconstructed by *sc*CAE agree well with PIV results at all monitoring points, demonstrating better prediction accuracies than those of CAE and *re*CAE for complex fluid flows around a cube. In brief, the *sc*CAE can not only capture the temporal evolution process of flow fields for all stages but also achieves an accurate reconstruction for full-field positions.

RMSEs of all instantaneous vector fields for test datasets $Re = 400$, 1000 and 1400 for flow around a cube are plotted in Figure 15. As shown in Figures 15a and 15b, RMSEs of both component velocities *U* and *V* reconstructed for fluid flows via *sc*CAE are much lower than those of CAE and *re*CAE for all extrapolated *Re*. This reflects that the ability of *sc*CAE on reconstructing time-sequence flow details for the cube is also robust. Meanwhile, low RMSEs of *sc*CAE for test datasets also reveal the proposed *sc*CAE has pretty good generalizability and extrapolation performances on feature extractions based on dimension reduction.

Thus, *sc*CAE proposed in this work is robust in capturing important features of fluid flows through dimension reduction, resulting in efficient representation of the flow characteristics with low-dimensional latent vectors. Based on the derived latent vectors, the time-resolved flow fields around a single sphere and cube at extrapolated *Re* of 400−1400, which typically display the high dimensional and nonlinear complex flow phenomena, can be successfully reconstructed using small datasets obtained via PIV measurements with noises.

4.5. Prediction of the Flow Fields. In the above sections, it is shown that feature extractions based on *sc*CAE perform well in reconstructing dynamic fluid flows for different *Re*, shapes and time-evolution information based on the small datasets obtained by PIV experiments with noises. The low-dimensional latent vectors, in which the most relevant features of the flow fields are conserved, may also be applied to the prediction of the evolutions of fluid flows over time based on small PIV datasets. In this section, we will test the performance of *sc*CAE in predicting time-resolved fluid flows around a single particle at various *Re* values.

https://doi.org/10.1021/acs.iecr.1c04704
Ind. Eng. Chem. Res. 2022, 61, 8504−8519

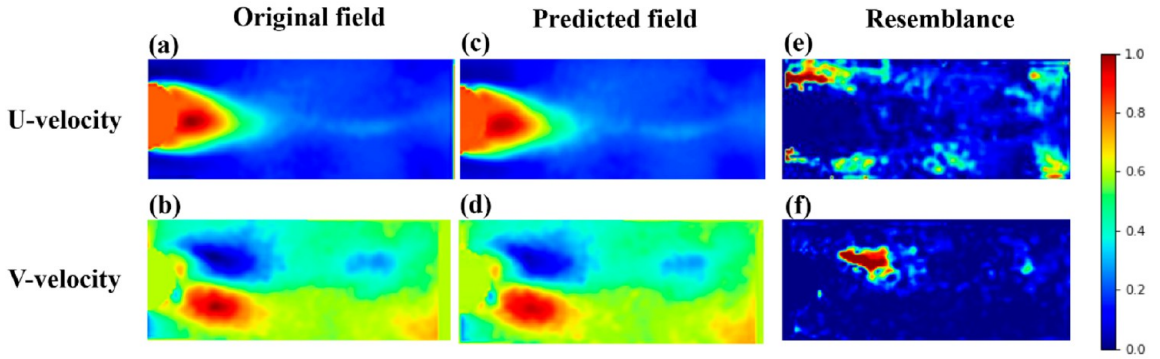

Figure 17. Visual prediction performances for the predicted 40th step by the *sc*CAE in the latent low-dimensional space alongside of original plots for flow around a sphere at *Re* = 600: (a) *U*-velocity of original field, (b) *V*-velocity of original field, (c) *U*-velocity of predicted field, (d) *V*-velocity of predicted field, (e) the likeness of *U*-velocity, (f) the likeness of *V*-velocity.

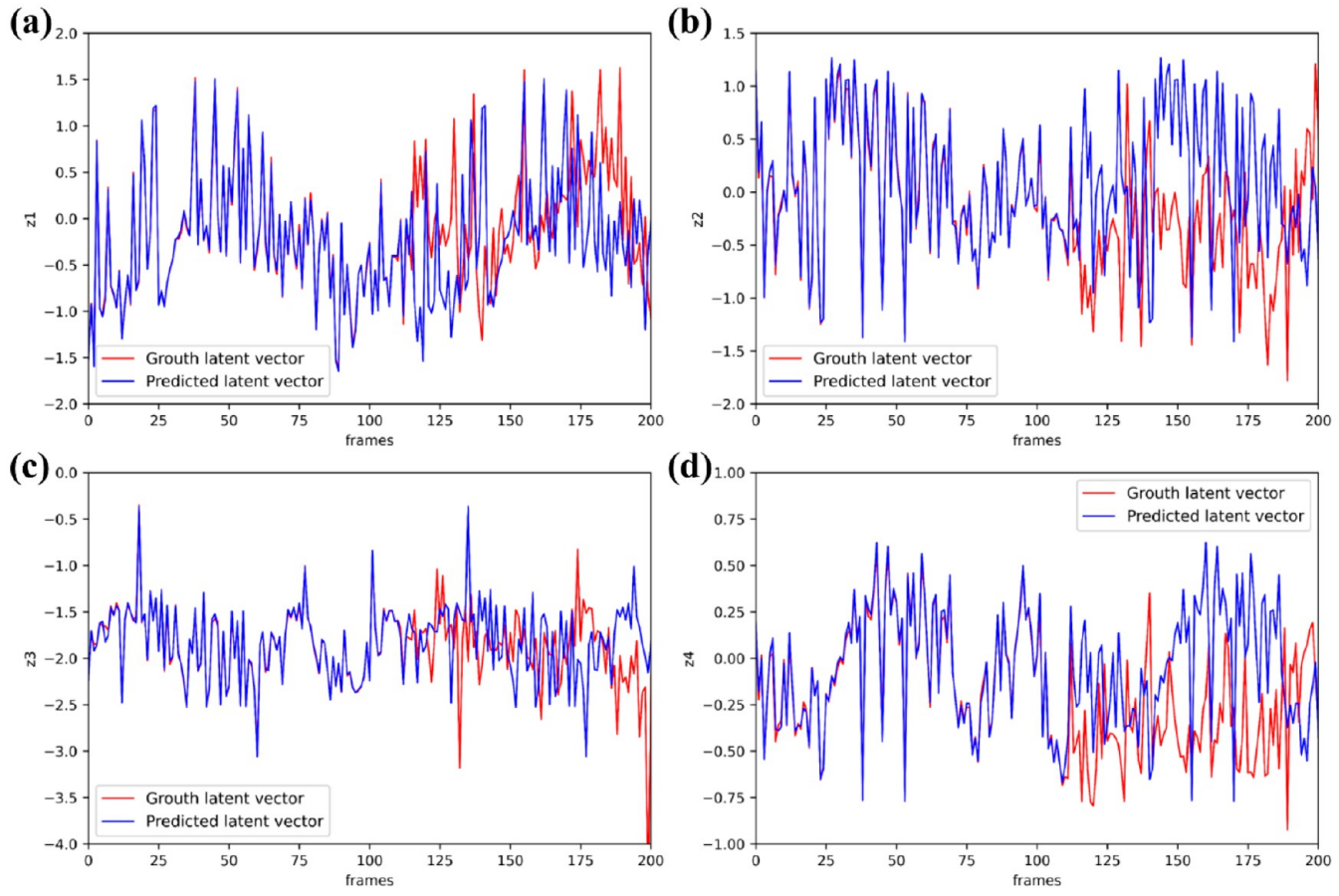

Figure 18. Comparisons of temporal evolutions along the four latent components between the original data (red) and the *sc*CAE prediction (blue) for flow around a cube at *Re* = 400: (a) the first latent component *z*1, (b) the second latent component *z*2, (c) the third latent component *z*3, (d) the fourth latent component *z*4.

For fluid flow around a single particle at a given *Re*, the time series of latent vectors obtained by *sc*CAE were used as the input of predicted CNN model to predict the future latent vectors, as was done by Agostini.[30] Once the predicted model is obtained, the latent vectors in 100 time step was used as the input and the output was time-series latent vectors predicted for the following 100 successive time steps. Figure 16 shows the four latent vectors *z*1−*z*4 for fluid flow around a sphere at *Re* = 600 for different time (denoted by the frames of fluid flow velocity fields). As can be seen, the predicted latent vectors (blue lines) can well collapse onto the actual latent vectors (red lines) for 40 successive time steps, illustrating that good prediction performances on time evolutions of flow fields could be achieved. We further showed the 40th frame of predicted vector fields of *U* and *V* around a sphere by using the predicted 40th latent vectors and the 39th vector field as inputs, as shown in Figure 17. The resemblance in our work represents the likeness between the reconstruction field and the original field measured by PIV, which is calculated via eq 7:

https://doi.org/10.1021/acs.iecr.1c04704
Ind. Eng. Chem. Res. 2022, 61, 8504−8519

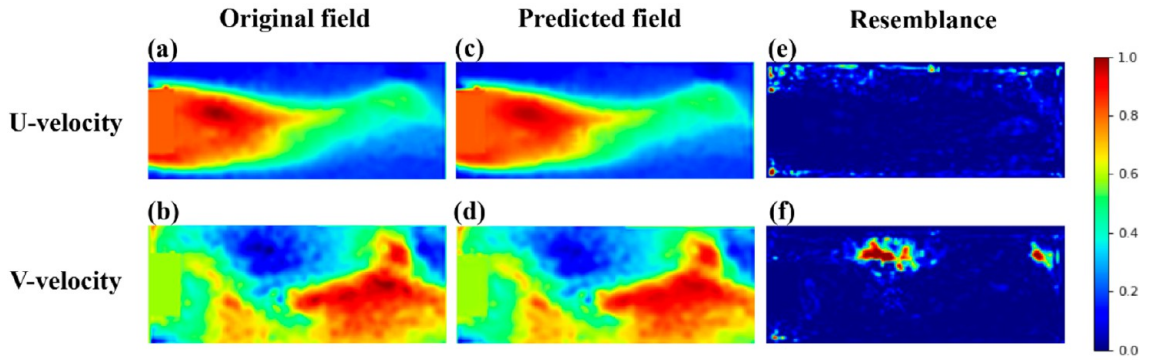

Figure 19. Visual prediction performances for the predicted 100th step by the *sc*CAE in the latent low-dimensional space alongside of original plots for flow around a cube at Re = 400: (a) U-velocity of original field, (b) V-velocity of original field, (c) U-velocity of predicted field, (d) V-velocity of predicted field, (e) the likeness of U-velocity, (f) the likeness of V-velocity.

$$\text{resemblance} = \left|1 - \left(2 \times \frac{|A \times B|}{(A^2 + B^2)}\right)^q\right| \tag{7}$$

where $A = u_{\text{PIV}} + \varepsilon$ and $B = u_{\text{predicted}} + \varepsilon$, with u_{PIV} representing U and/or V of the original PIV measured field, $u_{\text{predicted}}$ the U and/or V of the predicted flow field, ε an extremely low number to avoid $(A^2 + B^2) = 0$, q the factor of the likeness. In this work, ε is set as 0.000001 and q is fixed as 16. If resemblance = 0, it means the predicted vector field is exactly same as the vector filed obtained by PIV measurements. Obviously, it can be seen from Figure 17c that the predicted vector fields of U and V are highly consistent with the original PIV measurement results.

Then, for flow around a cube, the prediction of flow fields was also performed. Figure 18 shows typical predicted results of the latent vectors $z1-z4$ for Re = 400. As can be seen, a fairly good prediction accuracy for the following 100 successive time steps was achieved since the predicted latent vectors agree well with those directly obtained from PIV measurements. The 100th predicted latent vectors remapped to high dimensionality for the cube are also visualized in Figure 19, which shows a high consistency with the original PIV flow fields. This demonstrates the latent vectors in *sc*CAE could serve as a general and robust tool to extract the most important features in time-resolved flow fields of the highly nonlinear dynamic fluid flows around a single particle with different shapes for different Re. Most importantly, *sc*CAE works well for small datasets obtained by truth PIV measurements because of the excellent capabilities of dimensional reduction and characteristics representation.

5. CONCLUSIONS

In this work, we systematically studied the performances of three convolutional neural networks based autoencoders in dimension reduction and feature capturing by evaluating their extrapolation abilities in flow field reconstruction and prediction based on small noised PIV datasets. It is found that the *sc*CAE, which was proposed by incorporating the skip-connections to CAE, can accurately reconstruct the time-resolved flow fields around a single sphere or a cube under moderate Re of 400−1400. Essentially, an optimal latent vector size of four for the proposed *sc*CAE can well represent the high-dimensional and nonlinear fluid flows, showing the lowest RMSE for reconstructing vector fields. The comparison of training loss as a function of epoch also shows that *sc*CAE achieves the best stability and robustness, illustrating the latent vector with a small size in *sc*CAE can extract and compact the most important information in flow fields with a meaningful low-dimensional representation. Furthermore, it is also shown *sc*CAE has a good performance on flow prediction by capturing the most important features for the time-resolved high dimensional and nonlinear dynamic fluid flows.

In summary, the proposed *sc*CAE can serve as a general and robust tool to reconstruct and predict complex time-series flow phenomena based on limited noisy PIV measurement datasets, which may open a venue to extract the latent vectors from limited experimental data and disclose the inherent physics.

AUTHOR INFORMATION

Corresponding Authors

Jibin Zhou − *National Engineering Laboratory for Methanol to Olefins (MTO), Dalian Institute of Chemical Physics, Chinese Academy of Sciences, Dalian 116023, China*; Email: zhoujibin@dicp.ac.cn

Mao Ye − *National Engineering Laboratory for Methanol to Olefins (MTO), Dalian Institute of Chemical Physics, Chinese Academy of Sciences, Dalian 116023, China*; orcid.org/0000-0002-7078-2402; Email: maoye@dicp.ac.cn

Authors

Likun Ma − *National Engineering Laboratory for Methanol to Olefins (MTO), Dalian Institute of Chemical Physics, Chinese Academy of Sciences, Dalian 116023, China; University of Chinese Academy of Sciences, Beijing 100049, China*

Sina Kashanj − *Department of Mechanical Engineering, University of Alberta, Edmonton T6G 1H9, Canada*

Shuliang Xu − *National Engineering Laboratory for Methanol to Olefins (MTO), Dalian Institute of Chemical Physics, Chinese Academy of Sciences, Dalian 116023, China*

David S. Nobes − *Department of Mechanical Engineering, University of Alberta, Edmonton T6G 1H9, Canada*

Complete contact information is available at: https://pubs.acs.org/10.1021/acs.iecr.1c04704

Notes

The authors declare no competing financial interest.

https://doi.org/10.1021/acs.iecr.1c04704
Ind. Eng. Chem. Res. 2022, 61, 8504−8519

■ ACKNOWLEDGMENTS

This work is part of a research program financially supported by the National Natural Science Foundation of China under Grant No. 21991093 and the DICP I202135. We also thank the support of the scholarship from the University of Chinese Academy of Sciences (UCAS) for the Joint Training Program as a visiting scholar in University of Alberta. We thank the help of Associate Professor Chenggong Li (National Engineering Laboratory for Methanol to olefins (MTO), Dalian Institute of Chemical Physics, Chinese Academy of Sciences) for the direct numerical simulation of two-dimensional flow around a circle at Re = 40, which was used in the response to reviewers.

■ REFERENCES

(1) Karthik, G. M.; Buwa, V. V. Effect of particle shape on fluid flow and heat transfer for methane steam reforming reactions in a packed bed. *AIChE J.* **2017**, *63* (1), 366−377.
(2) Suresh, K.; Kannan, A. Effects of particle diameter and position on hydrodynamics around a confined sphere. *Ind. Eng. Chem. Res.* **2011**, *50* (23), 13137−13160.
(3) Krishnan, S.; Kannan, A. Effects of particle blockage and eccentricity in location on the non-newtonian fluid hydrodynamics around a sphere. *Ind. Eng. Chem. Res.* **2012**, *51* (45), 14867−14883.
(4) Khan, M. H.; Sooraj, P.; Sharma, A.; Agrawal, A. Flow around a cube for Reynolds numbers between 500 and 55,000. *Exp. Therm. Fluid Sci.* **2018**, *93*, 257−271.
(5) Klotz, L.; Goujon-Durand, S.; Rokicki, J.; Wesfreid, J. E. Experimental investigation of flow behind a cube for moderate Reynolds numbers. *J. Fluid Mech.* **2014**, *750*, 73−98.
(6) Eshbal, L.; Rinsky, V.; David, T.; Greenblatt, D.; van Hout, R. Measurement of vortex shedding in the wake of a sphere at Re = 465. *J. Fluid Mech.* **2019**, *870*, 290−315.
(7) Darabi, H.; Koleini, S. M. J.; Deglon, D.; Rezai, B.; Abdollahy, M. Particle image velocimetry study of the turbulence characteristics in an aerated flotation cell. *Ind. Eng. Chem. Res.* **2017**, *56* (46), 13919−13928.
(8) Deng, Z.; Chen, Y.; Liu, Y.; Kim, K., Time-resolved turbulent velocity field reconstruction using a long short-term memory (LSTM)-based artificial intelligence framework. *Phys. Fluids* **2019**, *31* (7), 075108 DOI: 10.1063/1.5111558.
(9) ten Cate, A.; Nieuwstad, C. H.; Derksen, J. J.; Van den Akker, H. E. A. Particle imaging velocimetry experiments and lattice-Boltzmann simulations on a single sphere settling under gravity. *Phys. Fluids.* **2002**, *14* (11), 4012−4025.
(10) Khan, M. H.; Sooraj, P.; Sharma, A.; Agrawal, A., Experimental investigation of flow around a 45o oriented cube for Reynolds numbers between 500 and 50000. *Phys. Rev. Fluids* **2021**, *6* (7). DOI: 10.1103/PhysRevFluids.6.074606
(11) Hajimirzaie, S. M.; Tsakiris, A. G.; Buchholz, J. H. J.; Papanicolaou, A. N. Flow characteristics around a wall-mounted spherical obstacle in a thin boundary layer. *Exp. Fluids* **2014**, *55* (6), 1762.
(12) Druault, P.; Guibert, P.; Alizon, F. Use of proper orthogonal decomposition for time interpolation from PIV data. *Exp. Fluids.* **2005**, *39* (6), 1009−1023.
(13) Schmid, P. J. Dynamic mode decomposition of numerical and experimental data. *J. Fluid Mech.* **2010**, *656*, 5−28.
(14) Murata, T.; Fukami, K.; Fukagata, K. Nonlinear mode decomposition with convolutional neural networks for fluid dynamics. *J. Fluid Mech.* **2020**, *882*, A13.
(15) Fukami, K.; Fukagata, K.; Taira, K. Assessment of supervised machine learning methods for fluid flows. *Theor. Comput. Fluid Dyn.* **2020**, *34* (4), 497−519.
(16) Rabault, J.; Kolaas, J.; Jensen, A., Performing particle image velocimetry using artificial neural networks: a proof-of-concept. *Meas. Sci. Technol.* **2017**, *28* (12).125301
(17) Cai, S.; Liang, J.; Gao, Q.; Xu, C.; Wei, R. Particle image velocimetry based on a deep learning motion estimator. *IEEE Trans. Instrum. Meas.* **2020**, *69* (6), 3538−3554.
(18) Yu, C.; Bi, X.; Fan, Y.; Han, Y.; Kuai, Y. LightPIVNet: an effective convolutional neural network for particle image velocimetry. *IEEE Trans. Instrum. Meas.* **2021**, *70*, 1−15.
(19) Yu, C.-D.; Fan, Y.-W.; Bi, X.-J.; Han, Y.; Kuai, Y.-F. Deep particle image velocimetry supervised learning under light conditions. *Flow Meas. Instrum.* **2021**, *80*, 80.
(20) Morimoto, M.; Fukami, K.; Zhang, K.; Nair, A. G.; Fukagata, K. Convolutional neural networks for fluid flow analysis: toward effective metamodeling and low dimensionalization. *Theor. Comput. Fluid Dyn.* **2021**, *35* (5), 633−658.
(21) Rawat, W.; Wang, Z. Deep convolutional neural networks for image classification: a comprehensive review. *Neural Comput.* **2017**, *29*, 1.
(22) Badrinarayanan, V.; Kendall, A.; Cipolla, R. SegNet: A deep convolutional encoder-decoder architecture for image segmentation. *IEEE Trans. Pattern Anal. Mach. Intell.* **2017**, *39*, 2481.
(23) Li, C.; Wand, M. In combining markov random fields and convolutional neural networks for image synthesis, *2016 IEEE Conference on Computer Vision and Pattern Recognition (CVPR)*, 2016.
(24) Kutz, J. N. Deep learning in fluid dynamics. *J. Fluid Mech.* **2017**, *814*, 1−4.
(25) Morimoto, M.; Fukami, K.; Zhang, K.; Fukagata, K. Generalization techniques of neural networks for fluid flow estimation. *Neural Comput. Applic.* **2022**, *216*, 3659−3669.
(26) Mohan, A. T.; Lubbers, N.; Livescu, D.; Chertkov, M., Embedding hard physical constraints in neural network coarse-graining of 3d turbulence. *arXiv preprint arXiv:2002.00021* 2020. (https://arxiv.org/abs/2002.00021).
(27) Omata, N.; Shirayama, S. A novel method of low-dimensional representation for temporal behavior of flow fields using deep autoencoder. *AIP Advances.* **2019**, *9* (1), 015006.
(28) Zhang, Y.; Sung, W. J.; Mavris, D. N., Application of convolutional neural network to predict airfoil lift coefficient. In *2018 AIAA/ASCE/AHS/ASC Structures, Structural Dynamics, and Materials Conference*; American Institute of Aeronautics and Astronautics. 2018, 1903.
(29) Hasegawa, K.; Fukami, K.; Murata, T.; Fukagata, K. Machine-learning-based reduced-order modeling for unsteady flows around bluff bodies of various shapes. *Theor. Comput. Fluid Dyn.* **2020**, *34* (4), 367−383.
(30) Agostini, L., Exploration and prediction of fluid dynamical systems using auto-encoder technology. *Phys. Fluids.* **2020**, *32* (6).067103
(31) Hochreiter, S. The vanishing gradient problem during learning recurrent neural nets and problem solutions. *Int. J. Unc. Fuzz. Knowl. Based Syst.* **1998**, *06* (02), 107−116.
(32) He, K.; Zhang, X.; Ren, S.; Sun, J. In deep residual learning for image recognition. *Proceedings of the IEEE conference on computer vision and pattern recognition* **2016**, 770−778.
(33) Wu, P.; Sun, J.; Chang, X.; Zhang, W.; Arcucci, R.; Guo, Y.; Pain, C. C. Data-driven reduced order model with temporal convolutional neural network. *Comput. Method. Appl. M.* **2020**, *360*, 112766.
(34) Mao, X. J.; Shen, C.; Yang, Y. B.Image restoration using very deep convolutional encoder-decoder networks with symmetric skip connections. In *NIPS'16: Proceedings of the 30th International Conference on Neural Information Processing Systems*, Barcelona, Spain, 2016; Lee, D. D., von Luxburg, U., Eds.; Curran Associates: Red Hook, NJ, 2016; *29*, pp 2802−2810.
(35) Ronneberger, O.; Fischer, P.; Brox, T. J. S. I. P. U-net: convolutional networks for biomedical image segmentation. *International Conference on Medical image computing and computer-assisted intervention.* **2015**, *9351*, 234−241.
(36) Thuerey, N.; Weißenow, K.; Prantl, L.; Hu, X. Deep learning methods for Reynolds-Averaged Navier-Stokes simulations of airfoil flows. *AIAA J.* **2020**, *58* (1), 25−36.

(37) Ioffe, S.; Szegedy, C. Batch normalization: accelerating deep network training by reducing internal covariate shift. In *Proceedings of the 32nd International Conference on International Conference on Machine Learning*, 2015; pp 448−456
(38) Nair, V.; Hinton, G. E. Rectified linear units improve restricted Boltzmann machines. In *Proceedings of the 27th International Conference on Machine Learning*, 807−814, Haifa, Israel, 2010.
(39) Fukami, K.; Fukagata, K.; Taira, K. J. J. o. F. M. Super-resolution reconstruction of turbulent flows with machine learning. *J. Fluid Mech.* **2019**, *870*, 106−120.
(40) He, K.; Zhang, X.; Ren, S.; Sun, J.Identity mappings in deep residual networks. In *Computer Vision − ECCV 2016*; European Conference on Computer Vision Series, Vol. *9908*; 2016, pp 630−645
(41) Le, Q. T.; Ooi, C., Surrogate modeling of fluid dynamics with a multigrid inspired neural network architecture. *arXiv preprint*, arXiv:2105.03854.
(42) Vogl, T. P.; Mangis, J.; Rigler, A.; Zink, W.; Alkon, D. Accelerating the convergence of the back-propagation method. *Biol. Cybern.* **1988**, *59* (4), 257−263.
(43) Kingma, D.; Ba, J., Adam: A method for stochastic optimization. *Comput. Sci.* 2014.
(44) Hasegawa, K.; Fukami, K.; Murata, T.; Fukagata, K. J. F. D. R. CNN-LSTM based reduced order modeling of two-dimensional unsteady flows around a circular cylinder at different Reynolds numbers. *Fluid Dyn. Res.* **2020**, *52* (6), 065501.

https://doi.org/10.1021/acs.iecr.1c04704
Ind. Eng. Chem. Res. 2022, 61, 8504−8519